

Asymmetric gaps of tetralayer graphene unveiled by thermodynamic characterization

Zhuangzhuang Qu(曲壮壮), Zhuoxian Li(李卓贤), Boxi Li(李博熙), Lipeng Hou(侯立芃), Xianghan Han(韩香岩), Qianling Liu(刘倩伶), Zhiyu Wang(王知雨), Kenji Watanabe, Takashi Taniguchi, Yanmeng Shi(史衍猛), and Jianming Lu(路建明)

Citation: Chin. Phys. B, 2025, 34 (**11**): 117201. DOI: 10.1088/1674-1056/adf9fc
http://cpb.iphy.ac.cn; http://iopscience.iop.org/cpb

What follows is a list of articles you may be interested in

High thermoelectric performance of SnS under high pressure and high temperature

Yuqi Gao(高语崎), Xinglin Wang(王星淋), Cun You(由存), Dianzhen Wang(王殿振), Nan Gao(高楠), Qi Jia(贾琪), Zhihui Li(李志慧), Qiang Tao(陶强), and Pinwen Zhu(朱品文)

Chin. Phys. B, 2025, 34 (**8**): 087201. DOI: 10.1088/1674-1056/addbc8

Emergence of correlations in twisted monolayer-trilayer graphene heterostructures

Zhang Zhou(周璋), Kenji Watanabe, Takashi Taniguchi, Xiao Lin(林晓), Jinhai Mao(毛金海), and Hong-Jun Gao(高鸿钧)

Chin. Phys. B, 2023, 32 (**9**): 097203. DOI: 10.1088/1674-1056/ace3a8

Interface-induced topological phase and doping-modulated bandgap of two-dimensioanl graphene-like networks

Ningjing Yang(杨柠境), Hai Yang(杨海), and Guojun Jin(金国钧)

Chin. Phys. B, 2023, 32 (**1**): 017201. DOI: 10.1088/1674-1056/ac904d

Observation of quadratic magnetoresistance in twisted double bilayer graphene

Yanbang Chu(褚衍邦), Le Liu(刘乐), Yiru Ji(季怡汝), Jinpeng Tian(田金朋), Fanfan Wu(吴帆帆), Jian Tang(汤建), Yalong Yuan(袁亚龙), Yanchong Zhao(赵岩翀), Xiaozhou Zan(昝晓州), Rong Yang(杨蓉), Kenji Watanabe, Takashi Taniguchi, Dongxia Shi(时东霞), Wei Yang(杨威), and Guangyu Zhang(张广宇)

Chin. Phys. B, 2022, 31 (**10**): 107201. DOI: 10.1088/1674-1056/ac6866

Group velocity matters for accurate prediction of phonon-limited carrier mobility

Qiao-Lin Yang(杨巧林), Hui-Xiong Deng(邓惠雄), Su-Huai Wei(魏苏淮), and Jun-Wei Luo(骆军委)

Chin. Phys. B, 2021, 30 (**8**): 087201. DOI: 10.1088/1674-1056/ac0133

RAPID COMMUNICATION

Asymmetric gaps of tetralayer graphene unveiled by thermodynamic characterization

Zhuangzhuang Qu(曲壮壮)[1,†], Zhuoxian Li(李卓贤)[1,†], Boxi Li(李博熙)[1,†], Lipeng Hou(侯立芃)[2,†], Xiangyan Han(韩香岩)[1], Qianling Liu(刘倩伶)[1], Zhiyu Wang(王知雨)[1], Kenji Watanabe[3], Takashi Taniguchi[3], Yanmeng Shi(史衍猛)[2,4,‡], and Jianming Lu(路建明)[1,§]

[1] *State Key Laboratory for Mesoscopic Physics, School of Physics, Peking University, Beijing* 100871, *China*

[2] *State Key Laboratory of Semiconductor Physics and Chip Technologies, Institute of Semiconductors, Chinese Academy of Sciences, Beijing* 100083, *China*

[3] *National Institute for Materials Science*, 1-1 *Namiki, Tsukuba, 305-0044, Japan*

[4] *Center of Materials Science and Optoelectronics Engineering, University of Chinese Academy of Sciences, Beijing* 100049, *China*

(Received 11 June 2025; revised manuscript received 21 July 2025; accepted manuscript online 11 August 2025)

Tetralayer graphene has shown several interesting properties such as tunable Lifshitz transitions, helical edge states, and high-temperature anomalous Hall effects. The band structure, which directly relates to these phenomena, has so far been predominantly determined by fitting Landau-level spectra. Here, by characterizing the electronic capacitance, we reveal unprecedented details of its band structure: the energy shift between the heavy- and light-mass band edges in the conduction band is much larger than that in the valence band. Their responses to displacement fields are also distinct: while the former increases monotonically and significantly, the latter first decreases and then increases slightly. Our results suggest that the interlayer interactions and hopping parameters are more complex than previously expected, calling for precise measurements of band structures in various multilayer van der Waals systems.

Keywords: quantum capacitance, band structure, Bernal tetralayer graphene, chemical potential

PACS: 72.80.Vp, 84.37.+q

DOI: 10.1088/1674-1056/adf9fc **CSTR:** 32038.14.CPB.adf9fc

1. Introduction

An anomalous Hall effect up to liquid-nitrogen temperature was recently observed in tetralayer graphene, attracting significant research interest in this largely unexplored material.[1,2] Compared with the linear/parabolic dispersion relation in monolayer/bilayer graphene,[3] the complex interlayer interaction leads to many unclarified details in the band structure of Bernal-stacked tetralayer graphene.[4–8] Briefly, Ref. [4] proposed an effective-mass model based on the Slonczewski–Weiss–McClure parametrization of graphite, where the system can be regarded as two bilayer graphenes with interlayer coupling.[6] The model was subsequently refined by fitting the Landau-level (LL) spectra to better account for the relaxed interlayer interaction between the outer and inner graphene layers.[5,6] It also successfully explained multiple Lifshitz transitions and helical edge states driven by perpendicular electric fields.[9,10] Despite these efforts, it remains unclear whether the fitting parameters accurately describe the band structure. Characterization using a method beyond the LL spectra is therefore highly desired.

In this work, by measuring the quantum capacitance, we reveal that the energy shifts between the heavy- and light-mass bands are distinct for the conduction and valence bands. The former exhibits a much larger magnitude than the latter. While the shift in the conduction band increases monotonically with displacement fields, that in the valence band first decreases and then increases. Our direct thermodynamic characterization of the band structures demonstrates that the interlayer interactions, and hence the hopping parameters, are more complex than previously determined, opening opportunities for precise measurements of band structures in van der Waals systems.

2. Methods

The number of graphene layers was identified by optical contrast,[11] and the stacking order of tetralayer graphene was confirmed by Raman spectroscopy.[12–15] The device was fabricated using standard dry-transfer methods.[16–18] All measurements were conducted in a cryostat at a base temperature of 2 K using lock-in techniques. Figure 1(a) shows the electrical measurement configuration, and we define the carrier density n and displacement field D as follows:

$$n = (C_{\rm b}V_{\rm b} + C_{\rm t}V_{\rm t})/e, \tag{1}$$

$$D = (C_{\rm b}V_{\rm b} - C_{\rm t}V_{\rm t})/(2\varepsilon_0). \tag{2}$$

†These authors contributed equally to this work.

‡Corresponding author. E-mail: ymshi@semi.ac.cn

§Corresponding author. E-mail: jmlu@lam.ln.cn

© 2025 Chinese Physical Society and IOP Publishing Ltd. All rights, including for text and data mining, AI training, and similar technologies, are reserved.

Here, $C_{t(b)}$ is the geometric capacitance per unit area between graphene and the top (back) gate, $V_{t(b)}$ is the gate voltage applied to the top (back) gate, e is the elementary charge, and ε_0 is the permittivity of vacuum.

3. Results and analysis

Figure 1(b) shows the two-dimensional projection $E(k_x)$ of the band structure, where the interlayer potential difference $U = 0$, i.e., $D = 0$. Here we used the hopping parameters following previous work:[9] $\gamma_0 = 3$ eV, $\gamma_1 = 0.39$ eV, $\Gamma_1 = 0.32$ eV, $\gamma_3 = 0.3$ eV, $\Gamma_3 = 0.25$ eV, $\gamma_4 = 0.04$ eV, $\Gamma_4 = 0.032$ eV, $\gamma_2 = -20$ meV, $\gamma_5 = 40$ meV, and $\delta_{AB} = 40.8$ meV, where δ_{AB} is the potential difference between dimer and non-dimer site atoms, γ terms involve one of the surface layers, and Γ terms involve only the inner or "bulk" layers. Bernal tetralayer graphene (BTG) undergoes successive Lifshitz transitions at three characteristic energies (ε_X, ε_Y, and ε_Z), manifested as abrupt changes in Fermi-surface topology with varying chemical potential.[9]

We first performed systematic transport measurements on the device. Figure 1(c) shows the four-terminal resistance map $R_{xx}(n,D)$ at 2 K and $B = 0$, where the prominent features are consistent with previous reports.[1,2,9] Figure 1(d) shows the Landau-fan diagram at $D = 0$ under weak magnetic fields, exhibiting multiple LL crossing patterns originating from two distinct bilayer-graphene-like band subsystems. The $B = 1$ T magnetotransport phase diagram in Fig. 1(e) reveals the most prominent quantum oscillations within the electron-doped region. Figure 1(f) identifies degeneracy factors of $g = 1/f = 2$ (valley-polarized metal) and $g = 4$ (isotropic metallic phase) through Fourier analysis of Shubnikov–de Haas oscillations in the low-field regime ($B < 2$ T). The observed transport characteristics collectively attest to the device's exceptional quality, thereby motivating the quantum capacitance measurements presented in the following section.

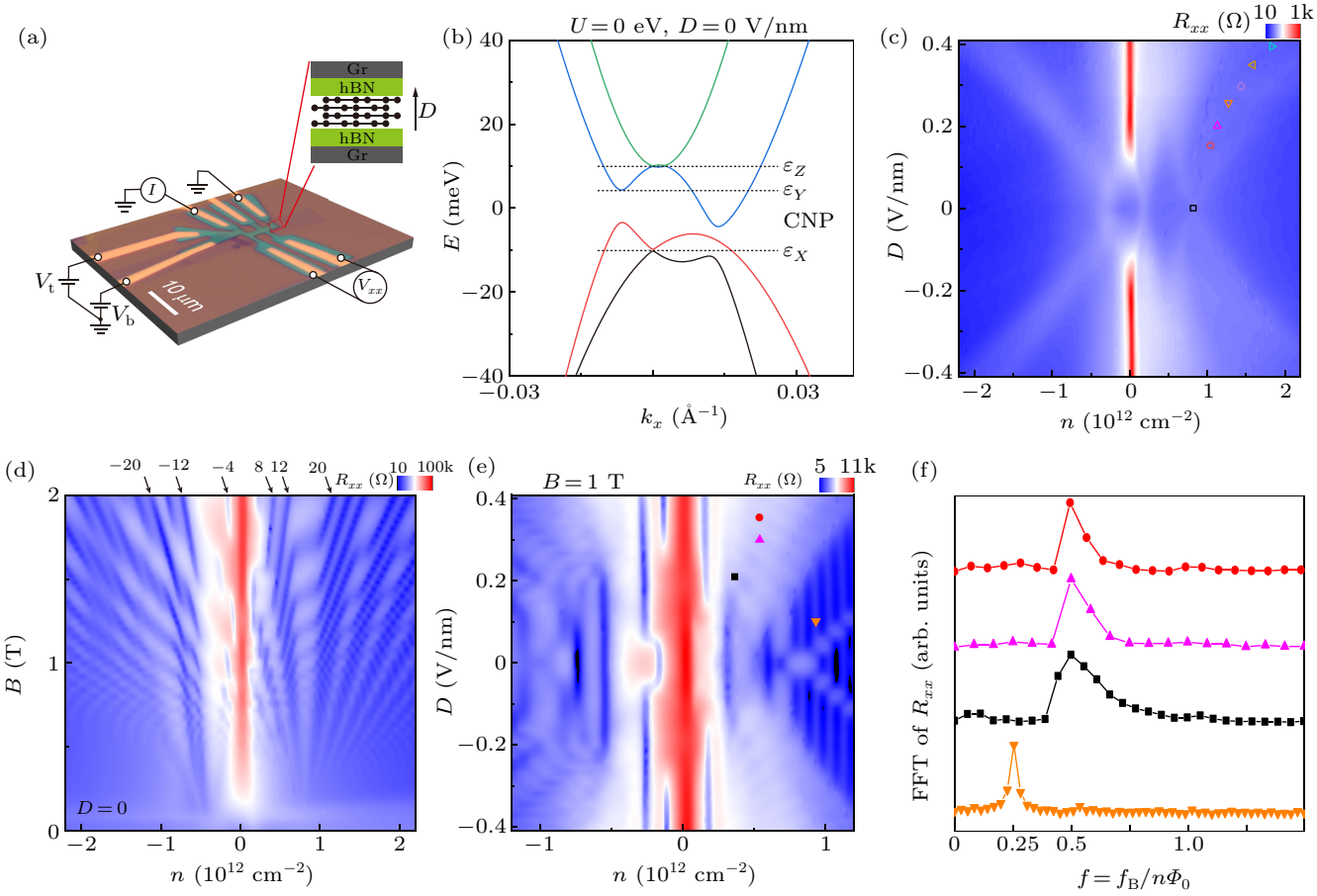


Fig. 1. Resistance measurements of Bernal-stacked tetralayer graphene at $T = 2$ K. (a) Device configuration. (b) Illustration of the band structure. (c) Resistance map as a function of carrier density n and displacement field D. The unfilled symbols correspond to the fixed points (n, D) in Fig. 3(b). (d) $R_{xx}(n,B)$ at $D = 0$. Numbers and arrows indicate filling factors. (e) $R_{xx}(n,D)$ at $B = 1$ T. (f) Fast Fourier transform (FFT) of $R_{xx}(1/B)$ (see Fig. S1 for details), measured at the fixed (n, D) points indicated by the corresponding symbols in (e). Data are plotted as $f = f_B/(n\Phi_0)$, where f_B is the oscillation frequency (in tesla) and $\Phi_0 = h/e$ is the magnetic flux quantum.

Figure 2(a) illustrates the quantum-capacitance measurement protocol using a capacitance bridge.[19–22] Initially, appropriate alternating current (AC) excitation voltages $\tilde{V}_{ref}$ and $\tilde{V}_{exc}$ are applied to the reference capacitance C_{ref} and the device, respectively, to balance the bridge. The excitation frequency is 68998.6 Hz and the amplitude is 10 mV (WF1974,

NF Corporation). The direct current (DC) biases V_T and V_{sam} control n and D, while $V_g = -0.05$ V and $V_{ds} = 4$ V (Keithley 2400) are fixed to operate the high-electron-mobility transistor (HEMT, FHX35X) in its optimal impedance-matching preamplifier regime. When equilibrium is disrupted, the resulting imbalance propagates through the HEMT, modulating the output voltage V_{out} (lock-in amplifier SR830). Figure 2(b) shows the capacitance ratio $\chi = C_s/C_{ref}$ as a function of the filling factor ν at $D = 0$ and $B = 9$ T. In the low-frequency limit, χ can be expressed as[22,23]

$$\frac{C_s}{C_{ref}} = \frac{A}{C_{ref}}\left(\frac{1}{C_t}+\frac{1}{C_b}+\frac{C_Q}{C_tC_b}\right)^{-1}+\frac{C_{para}}{C_{ref}}, \tag{3}$$

$$C_p = \left(\frac{1}{C_t}+\frac{1}{C_b}+\frac{C_Q}{C_tC_b}\right)^{-1}, \tag{4}$$

where C_s is the device capacitance, C_{ref} is the reference capacitance, A is the device area, C_Q is the quantum capacitance per unit area of BTG, C_p is the penetration-field capacitance per unit area, and C_{para} is the parasitic capacitance. Figure 2(b) highlights two distinct quantum capacitance regimes: χ_1 (compressible phase) and χ_2 (incompressible state), corresponding to the divergent ($C_Q \to \infty$) and vanishing ($C_Q \to 0$) limits of quantum capacitance, respectively. The finite density of states (DOS) results in the total device capacitance lying between these two extremes. Based on χ_1, χ_2, and Eqs. (3) and (4), we obtain

$$C_p = \frac{\chi-\chi_1}{\chi_2-\chi_1}\cdot\frac{C_tC_b}{C_t+C_b}, \tag{5}$$

$$C_Q = \frac{\chi_2-\chi}{\chi-\chi_1}\cdot(C_t+C_b). \tag{6}$$

Figure 2(c) displays C_p at $D = 0$ and $B = 3$ T. Distinct peaks emerge at filling factors $\nu = 4n$ ($n = 1, 2, 3, \ldots$), signaling minimized DOS at these quantum Hall states. Notably, the absence of C_p peaks at certain filling factors (e.g., $\nu = 12$ and 28) indicates enhanced DOS arising from LL crossings. Incorporating the quantum-capacitance contribution into the total capacitance, we derive the renormalized carrier density $\tilde{n}$ and the chemical-potential shift $\Delta\mu$

$$\tilde{n} = \frac{1}{e}\int\left(\frac{1}{C_t}+\frac{1}{C_Q}\right)^{-1}\mathrm{d}V_T - \frac{1}{e}\int\left[\left(\frac{1}{C_t}+\frac{1}{C_Q}\right)^{-1}+\left(\frac{1}{C_b}+\frac{1}{C_Q}\right)^{-1}\right]\mathrm{d}V_{sam}, \tag{7}$$

$$\Delta\mu = e\int\left(1+\frac{C_Q}{C_t}\right)^{-1}\mathrm{d}V_T - e\int\left[\left(1+\frac{C_Q}{C_t}\right)^{-1}+\left(1+\frac{C_Q}{C_b}\right)^{-1}\right]\mathrm{d}V_{sam}. \tag{8}$$

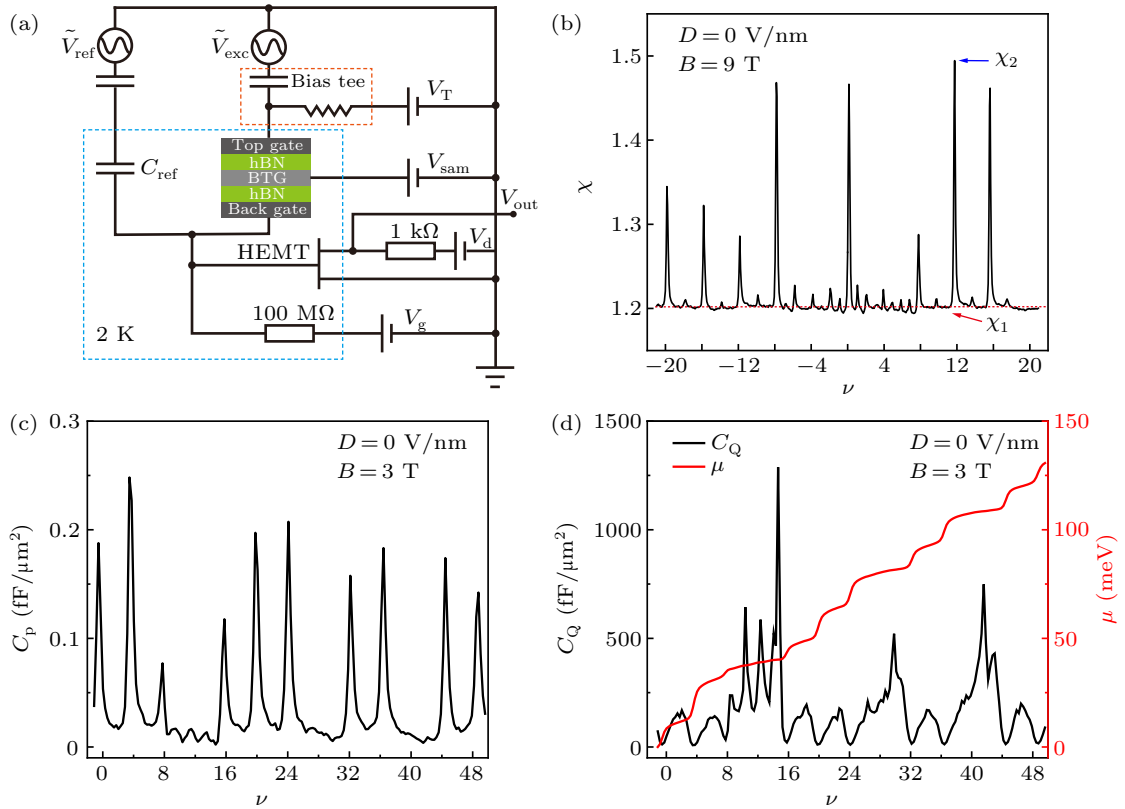


Fig. 2. Capacitance measurements. (a) Schematic of the capacitance bridge circuit. The combined signal of $\tilde{V}_{ref}$ and V_T is applied to the device through a bias tee. The reference capacitor consists of two parallel gold plates (30×30 μm^2 surface area, ~ 50 nm thickness) separated by 5 μm. A 100 MΩ series resistor prevents current drainage through the ground path of the capacitance bridge. (b) Capacitance ratio χ as a function of filling factor ν at $D = 0$ and $B = 9$ T. The arrows denoted as χ_1 and χ_2 indicate two extremes. (c) C_p calculated at $D = 0$ and $B = 3$ T. (d) Quantum capacitance C_Q and chemical potential μ at $D = 0$ and $B = 3$ T.

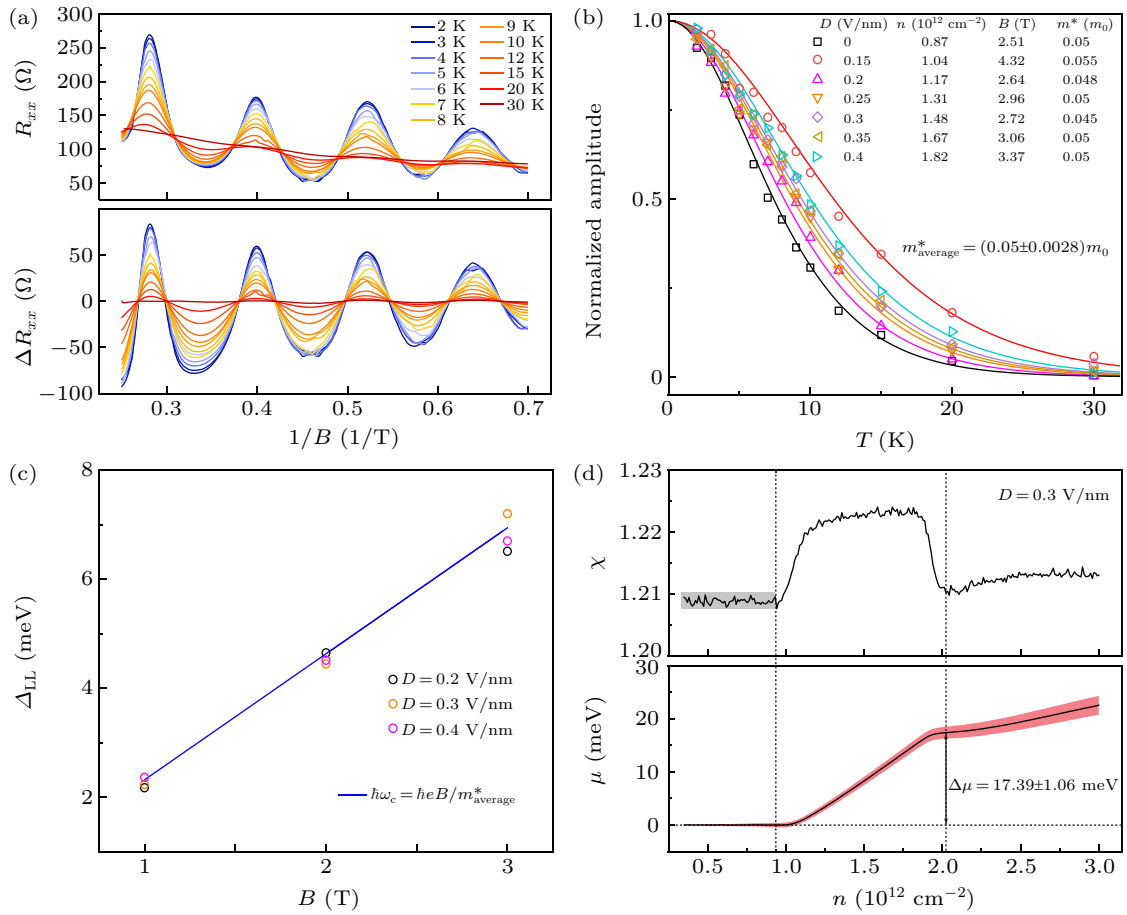


Fig. 3. Calibration between resistance and capacitance measurements. (a) Temperature-dependent quantum oscillations at $D = 0$ and $n = 0.87 \times 10^{12}$ cm^{-2}. The upper panel shows $R_{xx}(1/B)$, while the lower panel displays the data after background subtraction. (b) Lifshitz–Kosevich fits (solid lines) to the normalized oscillation amplitudes (symbols) at fixed points (n, D) labelled in Fig. 1(c). (c) LL gaps calculated from $\hbar\omega_c$ (blue) and from $\Delta\mu$ based on χ_{band} and $1.6\chi_2$ at three different D values (hollow circles) as a function of B. (d) Mean and standard deviation of χ within the shaded region (upper panel) are taken as χ_{band} and $\delta\chi$, respectively. The chemical potential μ (solid black line) is obtained by integrating C_{Q}, and the accumulated uncertainty from χ_{band} is represented by the shaded pink region.

Figure 2(d) presents the evolution of C_{Q} and μ at $D = 0$ and $B = 3$ T, correlated with the C_{p} data in Fig. 2(c). The observed anticorrelation between C_{Q} and C_{p} traces aligns precisely with the theoretical framework established in Eqs. (5) and (6). The chemical potential exhibits a characteristic staircase progression during electron filling: (i) Within the $4n$ ($n = 1, 2, 3, \ldots$) LL filling intervals, μ evolves gradually due to the elevated DOS between LLs; (ii) approaching integer filling factors $\nu = 4n$, abrupt variations in μ emerge concomitantly with the formation of LL energy gaps and the subsequent DOS collapse.

In practice, χ_1 and χ_2 are not appropriate boundary values for the precise calculation of C_{Q} and μ. We define χ in the compressible and incompressible limits as χ_{band} and χ_{gap}, respectively. The chemical potential we integrate lies on top of a background of non-constant compressibility, where the noise level is significant compared with the incompressible peaks. Thus, taking χ_1 as a global estimate for χ_{band} is not accurate under different conditions. We instead use a local background as χ_{band} for each integration at a fixed D. In the LL gap regime of BTG, the bulk remains insulating, while topologically protected conducting edge states emerge along the edges, exhibiting a finite yet non-vanishing DOS. Therefore, $\chi_{\text{gap}} > \chi_2$.

Based on the determination of χ_{band} and the discussion regarding χ_{gap}, and considering that the LL energy difference can be independently obtained from both theoretical formulas and chemical potential analysis, we determine the appropriate χ_{gap} by systematically adjusting its value to reconcile the LL energy differences derived from the chemical potential with those obtained from theoretical formulas. Before this procedure, we first acquire a crucial parameter: the effective mass (m^*). We select seven fixed points in the energy gap on the electron side to obtain m^*. Figure 3(a) presents temperature-dependent quantum oscillations at $D = 0$ and $n = 0.87 \times 10^{12}$ cm^{-2}. The upper panel displays $R_{xx}(1/B)$, while the lower panel shows the resistance after background subtraction. Lifshitz–Kosevich fitting (black solid line) of the normalized amplitudes of oscillations (black hollow squares) is shown in Fig. 3(b). The effective masses of these fixed points are listed, and the mean value of m^* is $0.05m_0$ (m_0 is the rest

mass of the electron), consistent with our theoretical calculation for the heavy-mass bands.[9] We employ $\Delta_{\mathrm{LL}} \approx \hbar\omega_{\mathrm{c}}$, $\omega_{\mathrm{c}} = eB/m^*$ to calculate the energy difference between adjacent LLs. We find that when $\chi_{\mathrm{gap}} = 1.6\chi_2$, the LL gap calculated from $\Delta\mu$ closely matches Δ_{LL}, as shown in Fig. 3(c). The chemical potentials at different D values under magnetic fields are shown in Figs. S2–S4. In Fig. 3(d), the mean value and standard deviation of χ within the shaded gray region, i.e., the local background, are calculated as χ_{band} and its corresponding uncertainty $\delta\chi$. The calculated chemical potential μ (black solid line) at $D = 0.3$ V/nm and $B = 0$ T is derived from χ_{band} and χ_{gap}. Error propagation in the integration process results in accumulated uncertainty (indicated by the gray shaded region), primarily originating from the uncertainty in χ_{band}.

Based on the preceding analysis, we present the $C_{\mathrm{p}}(n, D)$ and $C_{\mathrm{Q}}(n, D)$ maps in Figs. 4(a) and 4(b), respectively, which reveal a distinct electron–hole asymmetry. Incorporating dielectric screening effects, we identify a linear scaling relationship between U and D with $D \approx 5.6U/t$, where $t = 1$ nm is the thickness of tetralayer graphene.[9,10] Figure 4(c) displays the calculated band structure at $D = 0.3024$ V/nm, where three characteristic band gaps emerge: Δ_{e} (electron-like), Δ_{CNP} (charge neutrality point), and Δ_{hole} (hole-like). The evolution of these gap parameters with D is systematically examined in Figs. 4(d)–4(f), which compare the chemical potential shifts ($\Delta\mu$) with band structure calculations across different D values. At the CNP region, theoretical calculations predict the opening of a small band gap that saturates at ~ 3 meV for large D.[24] Our results, however, deviate from this trend, and the observed energy gap is too large for a sample with ~ 1 kΩ resistance at 2 K. We tentatively propose the following explanation: as illustrated in the inset of Fig. 4(d), inhomogeneities in doping and strain likely cause spatial variations in the Fermi level across different regions (upper inset), resulting in a finite DOS at the CNP (lower inset) and a significantly broadened energy "gap" around the CNP. Notably, this broadening effect around the CNP is expected to be suppressed in states with higher carrier densities because of Coulomb screening by charged impurities. For the electron-doped regime, our experimental findings show excellent agreement with theoretical predictions. Notably, the theoretically predicted energy gap evolution in the hole-doped regime exhibits an almost identical trend. However, our results display nonmonotonic evolution: the initial gap narrowing below 0.15 V/nm transitions to a gradual reopening at higher D. The distinct behaviors of the conduction and valence bands call for a re-examination of band structure calculations in future work.

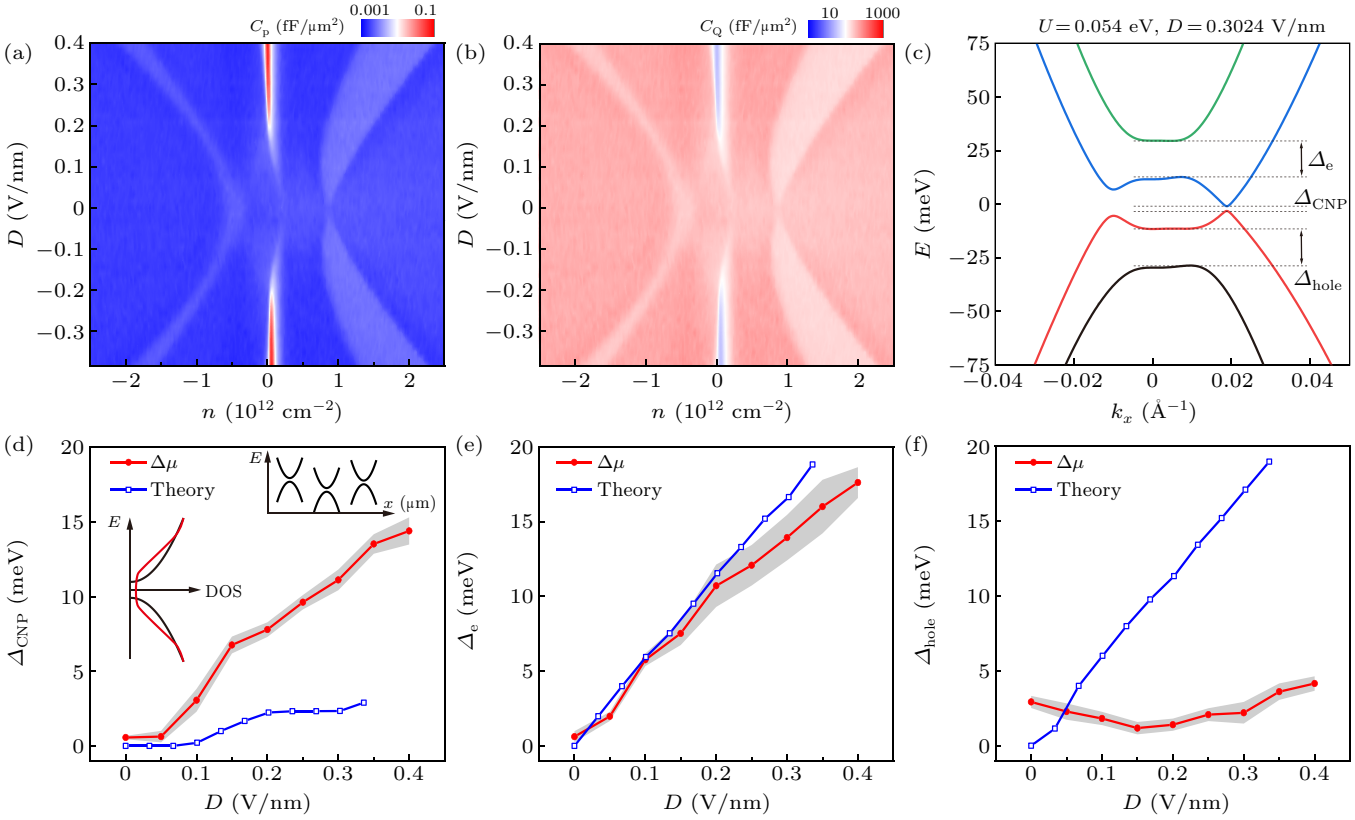


Fig. 4. Distinct energy gaps in the conduction and valence bands. (a) C_{p} mapping as a function of n and D. (b) Corresponding quantum capacitance C_{Q}. (c) Calculated band structure at $D = 0.3024$ V/nm, showing three characteristic gaps: Δ_{e} (electron-like), Δ_{CNP} (charge neutrality point), and Δ_{hole} (hole-like). (d)–(f) Comparison between experimental and calculated energy gaps at different D for the CNP (d), conduction band (e), and valence band (f). Gray shaded regions represent the uncertainty ranges (error bars).

4. Conclusion

In this work, we systematically characterized the quantum capacitance of Bernal tetralayer graphene and found that the energy gaps between the heavy- and light-mass band edges are distinct for the conduction and valence bands. The gap in the conduction band is significantly larger than that in the valence band. Moreover, while the conduction-band gap increases monotonically with increasing displacement field, the valence-band gap first decreases and then increases. Our direct thermodynamic characterization of the band structure reveals that the interlayer interactions — and consequently the hopping parameters — are more complex than previously determined. These results highlight the necessity of combining multiple measurement techniques to accurately resolve the band structures of multilayer van der Waals systems.

Acknowledgments

This work was supported by the National Natural Science Foundation of China (Grant Nos. 123B1037 and 12274402) and the National Key Research and Development Program of China (Grant No. 2024YFA1409700).

References

[1] Chen H, Arora A, Song J C W and Loh K P 2023 *Nat. Commun.* **14** 7925
[2] Qu Z, Chen Z, Han X, Wang Z, Li Z, Liu Q, Zhao W, Watanabe K, Taniguchi T, Cheng Z G, Gan Z and Lu J 2025 *Chin. Phys. B* **34** 037201
[3] Castro Neto A H, Guinea F, Peres N M R, Novoselov K S and Geim A K 2009 *Rev. Mod. Phys.* **81** 109
[4] Slonczewski J C and Weiss P R 1958 *Phys. Rev.* **109** 272
[5] Wu Z, Han Y, Lin J, Zhu W, He M, Xu S, Chen X, Lu H, Ye W, Han T, Wu Y, Long G, Shen J, Huang R, Wang L, He Y, Cai Y, Lortz R, Su D and Wang N 2015 *Phys. Rev. B* **92** 075408
[6] Koshino M and McCann E 2011 *Phys. Rev. B* **83** 165443
[7] Grushina A L, Ki D K, Koshino M, Nicolet A A L, Faugeras C, McCann E, Potemski M and Morpurgo A F 2015 *Nat. Commun.* **6** 6419
[8] Liang M, Li S and Gao J H 2022 *Phys. Rev. B* **105** 045419
[9] Shi Y, Che S, Zhou K, Ge S, Pi Z, Espiritu T, Taniguchi T, Watanabe K, Barlas Y, Lake R and Lau C N 2018 *Phys. Rev. Lett.* **120** 096802
[10] Che S, Shi Y, Yang J, Tian H, Chen R, Taniguchi T, Watanabe K, Smirnov D, Lau C N, Shimshoni E, Murthy G and Fertig H A 2020 *Phys. Rev. Lett.* **125** 036803
[11] Bing D, Wang Y, Bai J, Du R, Wu G and Liu L 2018 *Opt. Commun.* **406** 128
[12] Cong C, Yu T, Sato K, Shang J, Saito R, Dresselhaus G F and Dresselhaus M S 2011 *ACS Nano* **5** 8760
[13] Han X, Liu Q, Wang Y, Niu R, Qu Z, Wang Z, Li Z, Han C, Watanabe K, Taniguchi T, Song Z, Mao J, Han Z V, Gan Z and Lu J 2023 *Nano Lett.* **23** 6875
[14] Han X, Liu Q, Wang Y, Niu R, Qu Z, Wang Z, Li Z, Han C, Watanabe K, Taniguchi T, Song Z, Liu J, Mao J, Han Z, Chittari B L, Jung J, Gan Z and Lu J 2024 *Nano Lett.* **24** 6286
[15] Han X, Zou Y, Liu Q, Wang Z, Niu R, Qu Z, Li Z, Han C, Watanabe K, Taniguchi T, Dong B, Song Z, Mao J, Han Z, Cheng Z G, Gan Z and Lu J 2024 *Nat. Commun.* **15** 9765
[16] Wang L, Meric I, Huang P Y, Gao Q, Gao Y, Tran H, Taniguchi T, Watanabe K, Campos L M, Muller D A, Guo J, Kim P, Hone J, Shepard K L and Dean C R 2013 *Science* **342** 614
[17] Niu R, Han X, Qu Z, Wang Z, Li Z, Liu Q, Han C and Lu J 2023 *Chin. Phys. B* **32** 017202
[18] Ding D, Niu R, Han X, Qu Z, Wang Z, Li Z, Liu Q, Han C and Lu J 2023 *Chin. Phys. B* **32** 067204
[19] Ashoori R C, Stormer H L, Weiner J S, Pfeiffer L N, Pearton S J, Baldwin K W and West K W 1992 *Phys. Rev. Lett.* **68** 3088
[20] Hazeghi A, Sulpizio J A, Diankov G, Goldhaber-Gordon D and Wong H S P 2011 *Rev. Sci. Instrum.* **82** 053904
[21] Island J O, Cui X, Lewandowski C, Khoo J Y, Spanton E M, Zhou H, Rhodes D, Hone J C, Taniguchi T, Watanabe K, Levitov L S, Zaletel M P and Young A F 2019 *Nature* **571** 85
[22] Aronson S H, Han T, Lu Z, Yao Y, Watanabe K, Taniguchi T, Ju L and Ashoori R C 2025 *Phys. Rev. X* **15** 031026
[23] Dultz S C and Jiang H W 2000 *Phys. Rev. Lett.* **84** 4689
[24] Avetisyan A A, Partoens B and Peeters F M 2009 *Phys. Rev. B* **80** 195401